

Accretion driven turbulence in filaments II: Effects of self-gravity

S. Heigl,^{1,2*} M. Gritschneider,¹ A. Burkert,^{1,2}

¹*Universitäts-Sternwarte, Ludwig-Maximilians-Universität München, Scheinerstr. 1, 81679 Munich, Germany*

²*Max-Planck Institute for Extraterrestrial Physics, Giessenbachstr. 1, 85748 Garching, Germany*

Accepted XXX. Received YYY; in original form ZZZ

ABSTRACT

We extend our previous work on simulations with the code RAMSES on accretion driven turbulence by including self-gravity and study the effects of core formation and collapse. We show that radial accretion onto filaments drives turbulent motions which are not isotropic but radially dominated. In contrast to filaments without gravity, the velocity dispersion of self-gravitating filaments does not settle in an equilibrium. Despite showing similar amounts of driven turbulence, they continually dissipate their velocity dispersion until the onset of core formation. This difference is connected to the evolution of the radius as it determines the dissipation rate. In the non-gravitational case filament growth is not limited and its radius grows linearly with time. In contrast, there is a maximum extent in the self-gravitational case resulting in an increased dissipation rate. Furthermore, accretion driven turbulence shows a radial profile which is anti-correlated with density. This leads to a constant turbulent pressure throughout the filament. As the additional turbulent pressure does not have a radial gradient it does not contribute to the stability of filaments and does not increase the critical line-mass. However, this radial turbulence does affect the radius of a filament, adding to the extent and setting its maximum value. Moreover, the radius evolution also affects the growth timescale of cores which compared to the timescale of collapse of an accreting filament limits core formation to high line-masses.

Key words: stars:formation – ISM:kinematics and dynamics – ISM:structure

1 INTRODUCTION

Turbulent motions are a key feature in the highly complex dynamics of the interstellar medium (ISM) as demonstrated by the famous “Larson’s Laws” (Larson 1981). Line observations of molecular clouds show a direct correlation between size and molecular linewidth which is usually interpreted as a consequence of a Kolmogorov-like turbulent cascade from supersonic motions on the scale of a tens of parsec sized molecular cloud down to the sonic point on the scale of parsec sized filaments (Kolmogorov 1941; Kritsuk et al. 2013; Federrath 2016; Padoan et al. 2016). As density structures are formed by the collision of supersonic flows in the turbulent cascade, the transition from supersonic to subsonic motions is essential for setting the scale at which turbulence stops to dominate and the first subsonic density structures form.

Dust observations show that filamentary structure is

ubiquitous on parsec sized scales in star-forming, as well as quiescent, molecular clouds and directly associated with core formation in filaments with supercritical line-masses (André et al. 2010; Arzoumanian et al. 2011; André et al. 2014). The fact that these supercritical filaments show an increasingly supersonic internal velocity dispersion for larger line-masses, has been interpreted as a consequence of their gravitational collapse (Arzoumanian et al. 2013). However, molecular line observations have shown that some filaments are actually made up of bundles of velocity coherent subcomponents in the line-of-sight velocity called fibres (Hacar et al. 2013, 2018) which also form in numerical simulations (Smith et al. 2014; Moeckel & Burkert 2015; Clarke et al. 2017). While these subcomponents show trans- or subsonic linewidths, here relative motions create supersonic linewidths in spectrally low resolved superposition. Moreover, filaments which do not show any substructure are observed to be inherently subsonic (Hacar & Tafalla 2011; Hacar et al. 2016a).

Two methods have been proposed to explain the formation of fibres. On the one hand, simulations by Smith et al.

* E-mail: heigl@usm.lmu.de

(2016) showed that the subcomponents form first in collapsing clouds as a consequence of the turbulent cascade and are collected into individual filaments by large scale motions. This process is known as the "fray and gather" scenario. On the other hand, in the "fray and fragment" scenario proposed by Tafalla & Hacar (2015), the formation of fibres is explained by the sweep-up of residual motions inside a filament itself. Together with gravity, these motions concentrate material into subsonic velocity coherent entities in which core fragmentation takes place. Clarke et al. (2017) pointed out that this model relies strongly on the vorticity of the gas in order to work. If the vorticity of two nearby regions is anti-parallel, the resulting flow compresses gas to the interface between the regions and thus leads to an over-dense fibre.

As indicated by Hacar et al. (2016b), there are two distinct modes of turbulence. On the one hand, there is the classical microscopic turbulence where the density and velocity fields are continuous and isotropic as in the Kolmogorov model. On the other hand, the macroscopic turbulence observed in filaments containing fibres is created by multiple discrete overdensities with internal velocity dispersions of about the sound speed moving with supersonic motions relative to each other. However, care has to be taken in interpreting the observations of fibres. As noted by Zamora-Avilés et al. (2017) and Clarke et al. (2018), velocity coherent structures in position-position-velocity space do not necessarily represent physical density structures in position-position-position space.

Nevertheless, in the absence of a driving source, turbulent motions decay on the timescale of a crossing time (Mac Low et al. 1998; Stone et al. 1998; Padoan & Nordlund 1999; Mac Low 1999; Mac Low & Klessen 2004). This timescale can be very short for filaments if one assumes the driving scale is given by the filament diameter. In a first study (Heigl et al. (2018a), hereafter called paper I), we used an external accretion flow motivated by the filaments self-gravity to provide a driving source of turbulence. While we explored the effects of accretion driven turbulence on non self-gravitating filaments, we now take self-gravity and core formation into account. Observationally, accreting material is expected to flow along striations, weak filamentary density enhancements perpendicular to the filaments and aligned with the magnetic field, and have accretion rates of the order of $10\text{--}100 M_{\odot} \text{ pc}^{-1} \text{ Myr}^{-1}$ (Palmeirim et al. 2013; Cox et al. 2016) and infall velocities of the order of $0.25\text{--}1.0 \text{ km s}^{-1}$ (Kirk et al. 2013; Palmeirim et al. 2013). Independent of their formation process, we show that as long as a filament is embedded in surrounding material, self-gravity leads to a continuous inflow onto the filament which causes the creation of turbulent motions.

In the following sections, we first introduce the basic concepts that we apply to our model (section 2). Thereafter, we discuss the numerical set-up of our simulations (section 3). Then we present our findings (section 4) and discuss the implications for core formation (section 5). Finally, we summarize our findings (section 6).

2 BASIC CONCEPTS

This section presents the fundamental principles which we use to derive our models. We discuss the theoretical hydrostatic profile of filaments and how filaments behave in an ambient medium. Then we derive expected accretion rates onto filaments motivated by their self-gravity and how the accretion affects their radii. Finally, we present a simple model of how accreted kinetic energy is transformed into turbulent velocities and how they are able to add pressure support.

2.1 Hydrostatic equilibrium

We use the isothermal and hydrostatic equilibrium model of a filament with a density profile described by Stodólkiewicz (1963) and Ostriker (1964):

$$\rho(r) = \frac{\rho_c}{\left(1 + (r/H)^2\right)^2} \quad (1)$$

where r is the cylindrical radius and ρ_c is its central density. The radial scale height H is given by the term:

$$H^2 = \frac{2c_s^2}{\pi G \rho_c} \quad (2)$$

where c_s is the isothermal sound speed and G the gravitational constant. For our simulations we assume that the isothermal gas has a temperature of 10 K. With a molecular weight of $\mu = 2.36$ the isothermal sound speed is $c_s = 0.19 \text{ km s}^{-1}$. The critical line mass above which a filament will collapse under its self-gravity is calculated by integrating the profile to $r \rightarrow \infty$:

$$\left(\frac{M}{L}\right)_{\text{crit}} = \frac{2c_s^2}{G} \approx 1.06 \cdot 10^{16} \text{ g cm}^{-1} \approx 16.4 M_{\odot} \text{ pc}^{-1}. \quad (3)$$

Filaments with a lower line-mass than the critical value expand as long as there is no outside pressure. If one now assumes the filament is embedded in an ambient medium with a source of external pressure p_{ext} , the filament radius and line-mass are limited and one can introduce the parameter f_{cyl} which is a measure of how close to the critical value the filament is:

$$f_{\text{cyl}} = \left(\frac{M}{L}\right) / \left(\frac{M}{L}\right)_{\text{crit}}. \quad (4)$$

It varies from 0 for a non-existing filament to 1, where a filament has exactly its critical line-mass. As shown by Fischera & Martin (2012), the radius R of the filament is then given by the position where the internal pressure matches the external pressure and can be expressed as:

$$R = H \left(\frac{f_{\text{cyl}}}{1 - f_{\text{cyl}}}\right)^{1/2}. \quad (5)$$

Together with the relation between the central density ρ_c and the density on the boundary of the filament,

$$\rho_c = \frac{\rho(R)}{(1 - f_{\text{cyl}})^2}, \quad (6)$$

one can write the radius as function of the boundary density:

$$R = \left(\frac{2c_s^2}{\pi G \rho(R)} \left(f_{\text{cyl}}(1 - f_{\text{cyl}})\right)\right)^{1/2}. \quad (7)$$

For a given boundary density, the radius has a maximum at $f_{\text{cyl}} = 0.5$ with a symmetric drop-off to zero at $f_{\text{cyl}} = 0.0$ and $f_{\text{cyl}} = 1.0$. The boundary density $\rho(R)$ depends on the outside pressure and thus on the mechanism responsible for the pressure. One possible source of pressure is the thermal pressure of the surrounding medium itself. If the density on the outside of the surface is given by ρ_{ext} and the medium can be assumed to be isothermal with sound speed c_s , the pressure acting onto the surface is:

$$p_{\text{ext}} = \rho_{\text{ext}} c_s^2. \quad (8)$$

If both, the filament and the surrounding gas, have the same temperature then the boundary density $\rho(R)$ and the density of the surrounding gas are the same. Different temperatures however, lead to a jump in density in order to establish hydrostatic equilibrium.

2.2 Filament accretion

Another possible source of outside pressure is accretion of material onto the filament. We are particularly interested in accretion due to the gravitational potential of the filament itself. The gravitational acceleration of a cylindrical distribution of mass with a given line-mass M/L is (Heitsch et al. 2009):

$$a = -\frac{2GM/L}{r}. \quad (9)$$

The potential energy that a gas parcel with mass m loses in free-fall when starting with zero velocity at a distance R_0 and accreting to the filament radius R is given by integrating the acceleration over r :

$$E_{\text{pot}} = 2Gm(M/L) \ln\left(\frac{R_0}{R}\right) \quad (10)$$

This leads to the accretion velocity v_a at the surface R in the case of cylindrical free-fall:

$$\begin{aligned} v_a &= 2\sqrt{G(M/L) \ln\left(\frac{R_0}{R}\right)} \\ &= 1.1 \text{ km s}^{-1} \left(\frac{M/L}{16.4 \text{ M}_{\odot} \text{ pc}^{-1}}\right)^{1/2} \left(\frac{\ln(R_0/R)}{\ln(100)}\right)^{1/2}. \end{aligned} \quad (11)$$

Assuming a reasonable filament with a radius of order 0.1 pc and a large region of gravitational influence on the scale of a molecular cloud (a factor of a hundred times its own radius) allows us to estimate an upper limit on the accretion velocity. A filament at 10 K needs a line mass several times larger than the critical line-mass to achieve an inflow velocity of even Mach 10.0. In our simulations, we set the inflow velocity to a fixed value at the inflow boundary. As the simulated domain is relatively small compared to the filament itself and the filament is not massive enough to accelerate accreting gas over the time it takes to reach the filament, we can assume a constant accretion rate set by the radius of the inflow region R_0 and the density at that radius ρ_0 :

$$\frac{\dot{M}}{L} = 2\pi\rho_0 R_0 v_a. \quad (12)$$

This leads to a time-independent density profile outside of the filament,

$$\rho(r) = \rho_0 \frac{R_0}{r} \quad (13)$$

with the outside density at the filament radius R being

$$\rho_{\text{ext}} = \rho_0 \frac{R_0}{R}. \quad (14)$$

If the inflow onto the filament is fast enough, ram pressure will dominate over the isothermal boundary pressure. Comparing to Equation 8, this is the case if the inflow velocity is greater than the isothermal sound-speed. The total external pressure is then given by

$$p_{\text{ext}} = \rho_{\text{ext}} (c_s^2 + v_a^2) = \frac{\rho_0 R_0 c_s^2 (1 + \mathcal{M}_a^2)}{R}. \quad (15)$$

where \mathcal{M}_a is the Mach number of the accretion flow. The external pressure is balanced by the internal pressure of the filament at the position of the boundary. In addition to the thermal pressure, turbulent motions inside the filament could be able to exert an additional turbulent component, an assumption we test in this study. Together with a turbulent component, the pressure equilibrium can then be written as:

$$\rho(R) c_s^2 (1 + \mathcal{M}_t^2) = \frac{\rho_0 R_0 c_s^2 (1 + \mathcal{M}_a^2)}{R}, \quad (16)$$

where \mathcal{M}_t is the Mach number of the turbulent motions within the filament at the boundary. Solving for the boundary density and inserting the result into Equation 7 gives the radius of a filament with an additional accretion pressure and internal turbulent motions as:

$$R = \frac{2c_s^2 (1 + \mathcal{M}_t^2)}{\pi\rho_0 R_0 G (1 + \mathcal{M}_a^2)} (f_{\text{cyl}}(1 - f_{\text{cyl}})). \quad (17)$$

Although the radius evolution has now lost its dependence on the square root, the general shape of the curve remains unchanged. There still is a maximum at $f_{\text{cyl}} = 0.5$ which only differs in its maximum value. Note that for $G \rightarrow 0$, Equation 17 transforms to the non-gravitational counterpart of Equation A6.

2.3 Accretion driven turbulence

The analytical prediction of accretion driven turbulence is based on the energy budget of accreted kinetic energy being converted to turbulent energy and its subsequent dissipation. Following Elmegreen & Burkert (2010) and Klessen & Hennebelle (2010), the change in turbulent energy \dot{E}_t is given by the energy accretion rate \dot{E}_a and the energy dissipation \dot{E}_d :

$$\dot{E}_t = \dot{E}_a - \dot{E}_d = (1 - \epsilon)\dot{E}_a. \quad (18)$$

The energy accretion rate is given by the accreted kinetic energy

$$\dot{E}_a = \frac{1}{2} \dot{M} v_a^2 \quad (19)$$

and the energy loss through dissipation by

$$\dot{E}_d \approx \frac{E_t}{\tau_d} = \frac{1}{2} \frac{M \sigma^3}{L_d}, \quad (20)$$

where the turbulent energy is expected to decay on the timescale of a crossing time:

$$\tau_d \approx \frac{L_d}{\sigma}. \quad (21)$$

Elmegreen & Burkert (2010) also introduce the efficiency factor ϵ as fraction of accreted energy used to sustain the turbulent motions:

$$\epsilon = \left| \frac{\dot{E}_d}{\dot{E}_a} \right|. \quad (22)$$

Heitsch (2013) used this approach together with a driving scale of the filament diameter $L_d = 2R$ to calculate the velocity dispersion in dependence of inflow velocity:

$$\sigma = \left(2\epsilon R(t) v_a^2 \frac{\dot{M}}{M(t)} \right)^{1/3}. \quad (23)$$

For a linear evolution in time of the radius and mass, this relation predicts a constant level of velocity dispersion which is determined by the inflow velocity. While our simulations do find an equilibrium in velocity dispersion, we cannot match the scaling of the prediction. In contrast, our simulations show a linear relation of the density weighted velocity dispersion and inflow velocity as shown in paper I. Note, that any model for the scaling of velocity dispersion and inflow velocity or even an equilibrium is directly tied to the evolution of the radius. This is due to the fact that the energy dissipation rate depends on the crossing time. Rewriting the energy dissipation rate as

$$\dot{E}_d = \frac{1}{2} \frac{M\sigma^3}{L_d} = \frac{1}{2} \frac{\dot{M}\sigma^3 t}{2R(t)}, \quad (24)$$

all terms in Equation 18 depend on the mass accretion rate and can be simplified to

$$\sigma^2 = \alpha v_a^2 - \frac{\sigma^3 t}{2R(t)}. \quad (25)$$

Here we introduce the factor α to account for energy losses in the isothermal oblique accretion shocks at the surface of the filament where the turbulent motions are created. In order to reach an equilibrium velocity dispersion, all terms must be independent of time. This is only the case under two conditions. Either the radius grows linear in time as then the dissipation rate is constant or the radius evolves superlinear in time for which the last term vanishes at large timescales. This explains why we have an equilibrium in the non self-gravitational case as we find a linear time evolution of the radius. We revisit the equilibrium level and give an explanation for the scaling in the appendix. In the case including self-gravity discussed in this paper, the radius evolves as a complicated function of time (Equation 7) and core formation could impact the velocity dispersion substantially.

2.4 Effect of turbulence on radial stability

An important question that we want to answer is if turbulence can increase the stability of filaments. Previous studies modeled the effects of turbulence on the equation of state either by logatropic models based on the scaling relations of molecular clouds (Larson 1981) where $p_{\text{turb}} \sim \ln \rho$ (Lizano & Shu 1989; Gehman et al. 1996a,b; McLaughlin & Pudritz 1997; Fiege & Pudritz 2000a), or negative index polytropes, where the polytropic exponent is between zero and one, as is the case for Alfvénic turbulence (Maloney 1988; Fatuzzo & Adams 1993; McKee & Zweibel 1995). One could also assume that isotropic turbulence behaves as an additional

component to the thermal pressure and add it to the scale height:

$$H^2 = \frac{2c_s^2 (1 + \mathcal{M}_t^2)}{\pi G \rho_c}. \quad (26)$$

Integrating over the filament profile as done for Equation 3, leads to an adjustment of the critical line-mass:

$$\left(\frac{M}{L} \right)_{\text{crit}} = \frac{2c_s^2 (1 + \mathcal{M}_t^2)}{G}. \quad (27)$$

Thus, turbulence would be able to increase the maximum line-mass a filament could sustain. Note that this adjustment does not affect the formula for the radius in Equation 17 as the additional turbulent term not only enters directly over the scale height, but also over f_{cyl} and thus cancels out. However, an increased maximum line-mass would lead to an offset to the point of the maximum radial extent from the value 0.5 if plotted against the unadjusted maximum thermal line-mass. In addition, an increased stability would lead to a delayed collapse of cores in a filament as long as they do not dissipate their turbulence on a much faster timescale. Therefore, we will also directly test the impact of turbulence by investigating the radial evolution and core collapse in filaments.

3 NUMERICAL SET-UP

All our simulations were executed with the code RAMSES (Teyssier 2002) which uses a second-order Godunov scheme to solve the conservative form of the discretised Euler equations on an Cartesian grid. For our runs we applied the MUSCL scheme (Monotonic Upstream-Centred Scheme for Conservation Laws, van Leer (1977)) together with the HLLC-Solver (Harten-Lax-van Leer-Contact (Toro et al. 1994)) and the multidimensional MC slope limiter (monotonized central-difference (van Leer 1979)).

Our simulations cannot resolve the evolution of the molecular cloud and the detailed velocity dispersion inside the filament at the same time. Therefore we focus on a pre-set converging radial flow onto a self-gravitating, isothermal filament in the centre of the box. We use a 3D box with a periodic boundary condition in the x-direction and outflow boundaries in the other two directions. As RAMSES has no radial boundary we define a cylindrical inflow zone with a radius of the boxsize and a thickness of two cells from which we drive a radial inflow onto the central x-axis of the box. The inflow zone has a fixed density and inflow velocity which is continuously renewed every timestep. The inflow leads to a build-up of a filament with a radius which is limited by gravity. The periodic boundary prevents the filament from collapsing along its axis and prohibits the loss of turbulent motions. As the radius does not grow to large values, we can often optimize the resolution of our simulations and use a boxsize of 0.4 pc which is half as large as the standard boxsize used in paper I. Therefore, in order to keep the initial conditions equivalent to paper I, we double the outer boundary density for the majority of our simulations to a value of $\rho_0 = 7.84 \cdot 10^{-22} \text{ g cm}^{-3}$ which corresponds to about $2 \cdot 10^2$ particles per cubic centimeters for a molecular weight of $\mu = 2.36$. While we perform simulations for inflow Mach

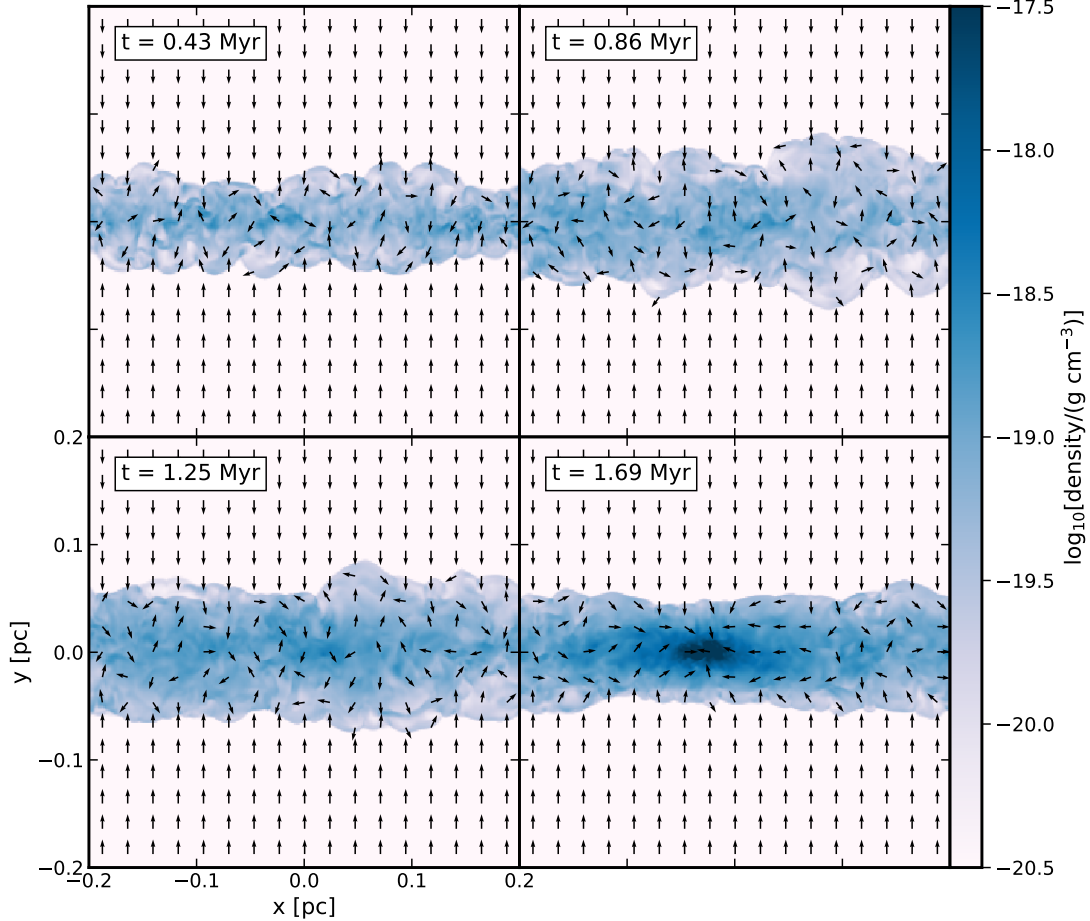


Figure 1. Evolution of an accreting filament with an inflow velocity of Mach 6.0 and an accretion rate of $8.4 M_{\odot} \text{ pc}^{-1} \text{ Myr}^{-1}$. The image shows four slices at different evolutionary times through the centre of the filament together with the directions of the local motion. In order to improve the contrast, we excluded the ambient medium from the colour bar. The cylindrical accretion induces obvious turbulent motions until a core is formed where the dominant velocity pattern changes to an accretion onto the core.

numbers ranging from 2.0 to 15.0, our analysis mainly concentrates on a reference case of a filament with an inflow velocity of Mach 6.0 or equivalently an mass accretion rate of $\dot{M}/L = 16.8 M_{\odot} \text{ pc}^{-1} \text{ Myr}^{-1}$ as the general results do not change with inflow velocity. We vary the mass accretion rate onto the filament by adjusting the boundary density and for simulations where we show the equilibrium level of turbulence, we reduce the density in the inflow region to a value which gives enough time to allow the equilibrium to settle without the filament collapsing. We also set the initial density inside the domain to the outer boundary density and vary the density in each cell with a random perturbation of 50%. The gas is set to be isothermal with a temperature of 10 K and the cells surrounding the inflow zone are given the same constant density and do not affect the simulation.

The minimum resolution is set to 256^3 , which at this boxsize is equivalent to the minimum resolution of about

0.002 pc used in paper I and guarantees that we resolve the filament across its diameter with a minimum of around 50 cells at all times. We employ adaptive mesh refinement (AMR) in order to resolve higher densities. Over the evolution of the simulation the filament stays unrefined and AMR only plays a role in the high density cores. The maximum resolution is set to 512^3 and in such a way that we terminate the simulation as soon as we do not fulfill the Truelove criterion for the maximum density within a factor of 16 in all simulations (Truelove et al. 1997).

4 SIMULATIONS

In this section we analyse the simulations in detail. While we concentrate on an inflow Mach number of 6.0, we performed the same analysis for all simulations ranging from

Mach 2.0 to 15.0 and the results are generally valid independent of inflow Mach number. As in paper I we study the velocity dispersion and radius of the filament. We show the typical evolution of a simulation in [Figure 1](#) where we plot slices through the central axis of the filament. As the filament grows in mass it first expands, reaches a maximum in radius and decreases again in radius. Towards reaching the critical line-mass of $f_{\text{cyl}} = 1.0$, usually one or more cores can be seen to condense inside the filament. Our simulation ends when we reach the maximum allowed density due to the Truelove criterion of around $10^{-17} \text{ g cm}^{-3}$ or 10^7 particles per cubic centimeter where we would need to insert a sink particle. As the subsequent core collapse happens on much shorter timescales than the evolution of the filament and we do not model expected feedback from protostellar outflows, we terminate our simulations as soon as we reach this threshold.

In comparison with the study of a similar set-up by [Clarke et al. \(2017\)](#) which used the Smooth Particle Hydrodynamic code GANDALF ([Hubber et al. 2018](#)), the density distribution inside the filament in our study is much smoother despite showing strong turbulent velocities. This is likely caused by the difference in initial conditions used by [Clarke et al. \(2017\)](#) which includes an initial turbulent velocity field in the accreting flow leading to larger substructures in the accreted material. In contrast, the turbulence in our study is generated by oblique shocks on the surface of the filament due to small-scale inhomogeneities on a cell-to-cell basis of the random perturbation in the accretion flow. The outcome reflects the distinction between the macroscopic and microscopic turbulent model mentioned in the introduction as we do not observe the formation of fibre-like structures in our simulations but rather small-scale and continuous turbulent density enhancements.

4.1 Evolution of the velocity dispersion

In order to calculate the velocity dispersion of the filament gas, we need to distinguish it from the accretion flow. Due to the formation of an accretion shock at the filament boundary, there is a clear jump in density and a drop in radial velocity of the material. However, the density inside the filament can vary considerably and therefore, instead of using an imprecise density jump criterion, we use the change in radial velocity as an indicator of filament material. We consider a cell to be part of the filament if its radial velocity with respect to the box centre has dropped to at least 0.9 of its boundary value as illustrated in [Figure 2](#). As the velocity jump is a very clear break, the calculated results do not depend strongly on the exact value of the velocity drop as it at most includes or excludes single cells which we confirm via a visual inspection of the filament material.

For the determination of the velocity dispersion in paper I, we used the standard deviation of the density weighted velocity:

$$u_i = \frac{m_i v_i}{\langle m \rangle} = \frac{N m_i v_i}{\sum m_i} = \frac{N m_i v_i}{M} \quad (28)$$

where N is the total number of cells and $\langle \rangle$ indicates the mean of a distribution. A more common way of defining the velocity dispersion of gas with zero mean velocity is by

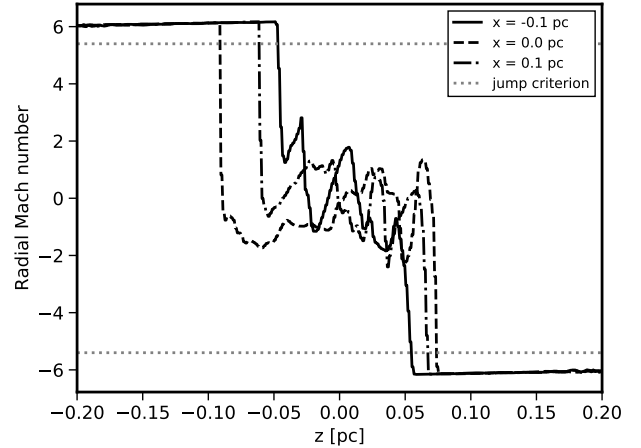


Figure 2. Example velocity cuts through the centre of the filament at different positions along the filament for a Mach 6.0 inflow. We define cells belonging to the filament when the radial velocity with respect to the box-centre falls below 0.9 times the boundary inflow velocity. This value is shown by the dotted gray lines. As one can see there is a strong drop in radial velocity as soon as the accretion flow reaches the filament edge.

calculating the total kinetic energy in the gas:

$$\sigma = \sqrt{\frac{1}{M} \sum_i m_i v_i^2}. \quad (29)$$

In the limit that the density is constant, both ways of calculating the velocity dispersion are equivalent as the velocity mean is zero and the standard deviation then is given by

$$\sigma_u = \sqrt{\langle u^2 \rangle - \langle u \rangle^2} = \sqrt{\frac{N^2 \sum_i m_i^2 v_i^2}{N M^2}} = \sqrt{\frac{m_i \sum_i v_i^2}{M}} \quad (30)$$

where we use the definition of the total mass $M = N m_i$. As the density inside a filament is not constant in our simulations, we expect different measured values of the velocity dispersions for the different methods. Especially for large values of turbulence the differences should increase as more and more shocks form inside the filament with larger density contrasts. For this study we use the method of the total kinetic energy ([Equation 29](#)).

In paper I we observed that without self-gravity of the filament gas, the velocity dispersion settles to a constant equilibrium value over time. This behavior was also found in the study by [Clarke et al. \(2017\)](#) which already included gravity. We want to test if it is possible to reproduce the transition to equilibrium if we include self-gravity in RAMSES. We measure the velocity dispersion of the filament gas for the same inflow velocity of Mach 6.0 but for different mass accretion rates and plot the evolution in [Figure 3](#). The black dashed-dotted line is the evolution of the velocity dispersion of the non-gravitational case which has the same mass accretion rate as our reference case of $16.8 M_{\odot} \text{ pc}^{-1}$. It ends in the same equilibrium value of an inflow velocity of Mach 6.0 presented in paper I.

The solid light blue curve shows a filament with an accretion rate which is ten times lower than that of the reference case and the non-gravitational case. In contrast to the

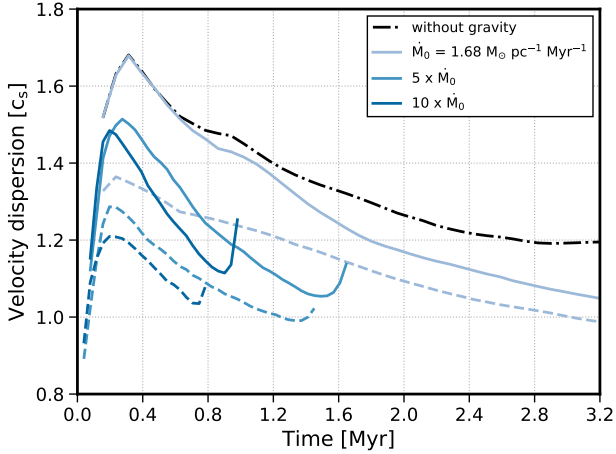


Figure 3. Evolution of the velocity dispersion for a Mach 6.0 inflow with varying accretion rate. We include a filament without gravity given by the dashed-dotted line as a reference case. The solid lines show filaments with different accretion rates. The dashed lines are the same initial values but with a pre-existing $1/r$ profile inside the box which smooths out the initial accretion shock.

non-gravitational case, the velocity dispersion continuously drops off even if we continue the simulation to larger times. If we increase the mass accretion rate by a factor of five, as given by the medium blue line, or a factor of ten, as given by the dark blue line, the velocity dispersion drops off even faster and ends when core formation sets in where the velocity dispersion increases due to collapse motions onto the core. We use the high inflow rate case as our fiducial case for further analysis.

We also test if our initial condition influences the evolution of the velocity dispersion. Therefore, we change our initial density profile in the box from a flat distribution to a $1/r$ profile, consistent with Equation 13 as if the accretion flow has already been established. The corresponding lines are shown in Figure 3 by the dashed lines. We see that it removes the initial spike in velocity dispersion. For higher accretion rates the initial value from where the velocity dispersion decays is lower but we also do not reach an equilibrium value.

We also split up the velocity dispersions into its cylindrical components by splitting the respective velocities into the x-component along the filament axis, the azimuthal and the radial velocities. Their evolution is shown in Figure 4 together with the Cartesian y and z component of the velocity dispersion. One can see that the turbulent motions are dominated by the radial velocity component and also only decay in the radial component while the other two stay constant over time. This is due to the difference in crossing times. Not only is the initial radial dispersion more than twice as large as the other components but it has also the lowest driving scale, with the azimuthal driving scale being a factor π larger and the driving scale along the filament being the boxsize in theory.

Therefore, albeit seeing an equilibrium velocity dispersion in filaments without gravity, gravitational collapse does influence the velocity dispersion by reducing it over time un-

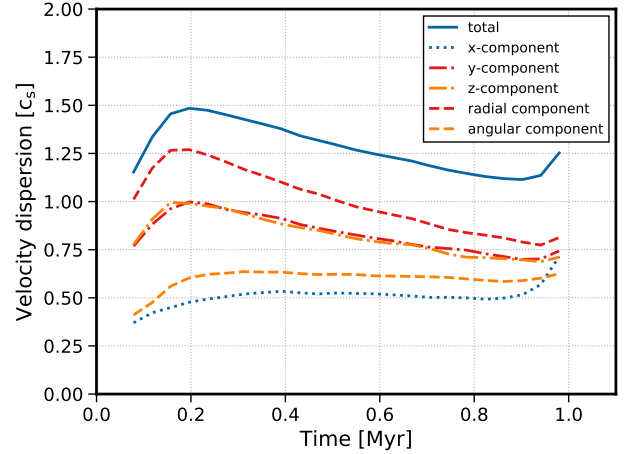


Figure 4. Evolution of the velocity dispersion of all components for a Mach 6.0 inflow with mass accretion rate of $16.8 M_{\odot} \text{ pc}^{-1} \text{ Myr}^{-1}$. The total velocity dispersion is shown by the blue solid line, the Cartesian components in y and z direction by the red and orange dashed-dotted lines and the cylindrical components in radial direction and in angular direction by the dashed red and orange lines respectively. The x-component, which is valid for both geometries is given by the blue dotted line.

til the point of core collapse where collapse motions increase it again. This result is in agreement with Equation 25, as for the non self-gravitational case, the radius evolves linearly, setting a constant dissipation rate and allowing for the velocity dispersion to settle to an equilibrium value. However, for self-gravitational filaments the radius has a maximum value and decreases again for large line-masses. This leads to a constant change in dissipation rate and thus no equilibrium can be achieved.

4.2 Radial evolution

We showed that in the non self-gravitational case, the radius evolves linearly in time and is supported by the radial turbulent motions (see also Appendix A). According to Equation 7, the radial expansion is limited in the self-gravitational prediction, reaching a maximum at $f_{\text{cyl}} = 0.5$, followed by a subsequent decrease. In order to assess the impact of turbulent motions on the radial extent, we compare Equation 17 to the measured radius. If turbulence has an impact on the scale height, one would see an off-set in the radius maximum. This off-set can be substantial, e.g. a factor of two in the case where the velocity dispersion is larger than the order of the sound speed. Thus, by measuring the radial evolution, we can not only test the impact of turbulence on the radius but also if it acts as additional pressure support.

Before we compare the measured radius to Equation 17, we have to determine the turbulent Mach number at the filament boundary, as \mathcal{M}_t in the above equation is not the total Mach number, but the one determining hydrostatic equilibrium at the boundary. In order to do so, we have to calculate the radial profile of the turbulent Mach number. For large accretion rates the filament is too thin to determine a reasonable radial profile. Thus, we increase the resolution by re-simulating our fiducial case with a four times smaller box

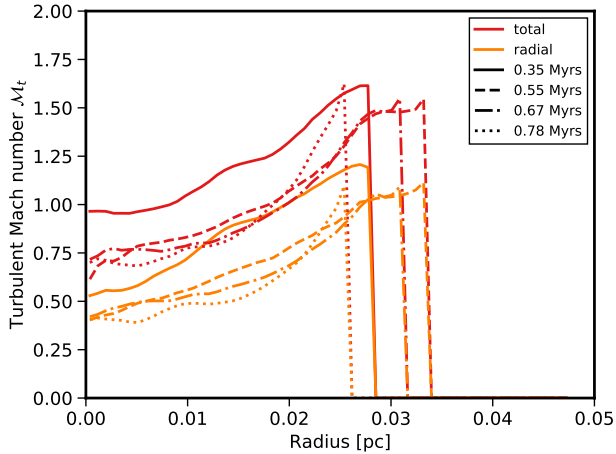


Figure 5. Turbulent Mach number averaged in radial bins of our fiducial filament with a Mach 6.0 accretion flow and an accretion rate of $16.8 M_{\odot} \text{ pc}^{-1} \text{ Myr}^{-1}$ measured at different timesteps given by the different linestyles. The total velocity dispersion is shown in and the radial velocity dispersion in orange.

with a size of 0.1 pc. As the inflow region has a $1/r$ density profile, we also have to increase the inflow density by a factor of four in order to only simulate a zoomed-in sub-volume. This guarantees us the same inflow conditions and accretion rate on a smaller scale. We take each slice of the filament, split the domain in radial bins with a width of 4 cells and thus a physical bin size of $1.5 \cdot 10^{-3}$ pc, subtract the mean velocity of the bin, determine the total kinetic energy in the bin and finally average over all slices along the filament. The result is shown in Figure 5, where we plot both, the Mach number of the total velocity dispersion in red and the Mach number of the radial velocity in orange, for several different timesteps distinguished by the different linestyles. As one can see, the velocity dispersion is not constant throughout the filament, but is minimal at the filament centre and has its maximum at the boundary. This shows how turbulent motions are stirred at the surface of the filament and dissipate in the higher density layers. Over time, it is the high density interior which loses significantly in turbulent velocities. In order to calculate the predicted radius we need to use the boundary value. In principle, one would need to determine this value at every time step but we do not see a significant change of the boundary value and it stays close to constant over time. We use both boundary values, the total and the radial Mach number, in Equation 17 and plot the predicted radius as well as the average measured radius against the average line-mass in Figure 6. As its value varies along the filament as can be seen from Figure 2, the radius itself is measured similar as the average of every slice along the filament.

The measured radial evolution is shown by the solid red line, the case of no turbulent support as the dashed curve, the case of radial turbulent pressure support as the dashed-dotted line and the case of total turbulent pressure support as the dotted curve. The measured radius follows closely the radial turbulent support model. Note, that the same is true in the non self-gravity case in Figure A1. Only the radial motions contribute to the hydrostatic equilibrium. One

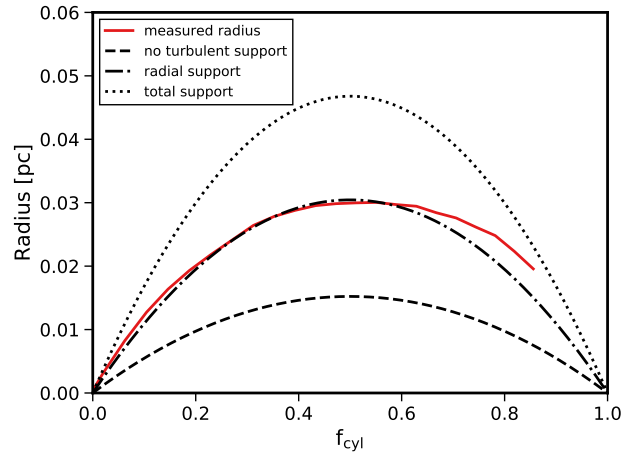


Figure 6. Evolution of the measured average radius of a filament with a Mach 6.0 accretion flow and an accretion rate of $16.8 M_{\odot} \text{ pc}^{-1} \text{ Myr}^{-1}$ compared to the average line-mass. The curve ends as soon as the core reaches the critical line-mass and collapses. The analytical evolution of the radius (Equation 17) without turbulent pressure contribution is shown by the dashed line, with radial turbulence support as the black dashed-dotted line and with total turbulence support as the black dashed-dotted line.

can see that the curve reaches its maximum value at about $f_{\text{cyl}} = 0.5$. It is important to note, that while turbulence does influence the maximum radius, it does not, or at most only marginally, affect the maximum line-mass and thus the point of where the radius reaches its maximum. According to Equation 27, we would expect a maximum line-mass of twice the isothermal maximum mass given the velocity dispersion created by an inflow velocity of Mach 6.0. Thus, the radial evolution should peak at a unadjusted value of about $f_{\text{cyl}} = 1.0$. Therefore, there is no indication of radial pressure support against gravity by turbulence as is consistent with the radial collapse discussed in the next section.

4.3 Core collapse

We showed that turbulence does not have an effect on where the radial evolution has its maximum with respect to the filament line-mass. Therefore, we assume that there is no additional support against radial collapse which we test by analysing the growth of the forming core and whether or not it collapses at the critical line-mass. We plot the line-mass at the position of the core against time in Figure 7. In Heigl et al. (2016) we showed that the radial collapse of the core is visible in the non-linear evolution of the line-mass. If turbulence indeed plays a role for the stability of a filament, we expect an offset from $f_{\text{cyl}} = 1.0$ with respect to the line-mass growth change from linear to non-linear. If we adapt Equation 27, we predict a shift in the critical line-mass to at least double the usual value for turbulent Mach numbers of the same order as the sound speed. As one can see from the form of the curves, a non-linear evolution sets in as soon as the local line-mass at the position of the core exceeds the critical line-mass determined without turbulent support. This shows again that turbulence in our simulations

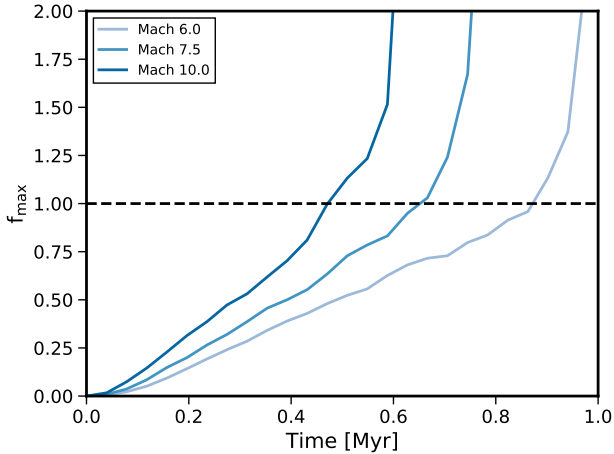


Figure 7. Time evolution of the maximum line-mass for different inflow Mach numbers. Due to the increasing mass in the filament, the maximum line-mass grows linearly. As soon as it reaches the unmodified critical line-mass at a value of 1.0, the core at this position collapses radially as can be seen in the non-linear evolution.

does not have a supporting effect on the line-mass, consistent with the findings of the radial evolution.

4.4 Why is there no pressure support?

In order to determine why there is no pressure support, we analyse the pressure profile of our high resolution fiducial filament as we did for the turbulent Mach number in Figure 5. We distinguish between cells that are part of the filament and others which trace the accretion flow by using the same method of determining the filament radius by the jump in radial velocity as mentioned above. As the filament radius is not uniform as can be seen in the example cuts in Figure 2, there is an overlap region where cells of both regions are present. We calculate the respective pressures with cells of the respective region and cells only contribute to the respective pressure on an individual basis. For the turbulent pressure we use only cells tracing the filament and determine the average density and kinetic energy in each bin i from which we calculate the pressure as $\langle \rho_i \rangle \sigma_i^2$ and then average over all slices. For the ram pressure we determine the average density and radial velocity in the accretion flow and calculate the ram pressure as $\langle \rho_i \rangle \langle v_i^{\text{rad}} \rangle^2$ and then average over all slices. The resulting pressure components are shown in Figure 8. The thermal pressure is given by the black dashed line, the ram pressure by the black dotted line, the total and radial turbulent pressure by the red and orange dashed-dotted line respectively and the combined thermal plus turbulent pressure by the respective solid line. The overlap region is illustrated by the dotted ram pressure line extending into the filament pressure over a broad range around the mean radius of about 0.03 pc.

We already showed in the last subsection that the radial turbulent motions provide the hydrostatic equilibrium together with the ram pressure. This can be seen also in the pressure directly, where the combined thermal plus ra-

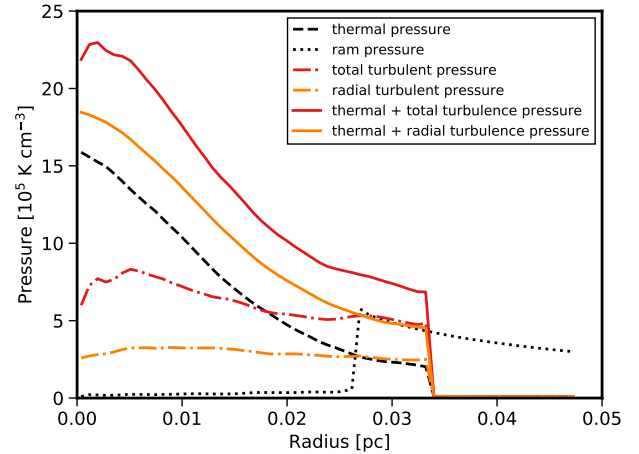


Figure 8. The different pressure contributions averaged in radial bins of our fiducial filament with an accretion flow of Mach 6.0 and an accretion rate of $16.8 M_{\odot} \text{ pc}^{-1} \text{ Myr}^{-1}$ measured at 0.5 Myrs. The black dashed line shows the thermal pressure of the filament gas and the black dotted line the ram pressure in the accretion flow. The turbulent pressure is given by the dashed-dotted lines and the sum together with the thermal pressure to show the total filament pressure by the solid lines: for the total velocity dispersion in red and for the radial velocity dispersion in orange.

dial turbulent pressure given by the orange solid line exactly balance the ram pressure in the overlap region. In contrast, the total turbulent pressure provides a pressure which is too large for an equilibrium. Moreover, one can see that the accretion driven turbulence, given by the dashed-dotted lines, distributes itself over the filament in a way that the turbulent pressure component is constant throughout the filament. In the context of large-scale in comparison to small-scale turbulence discussed in the introduction, it seems to resemble the classical Kolmogorov model as it does not form overdense regions of different levels of turbulence. This leads to the fact that the pressure profile of the filament is only shifted to an overall larger pressure by a constant value due to turbulence as can be seen in the figure by comparing the dashed black and the solid orange line. One can interpret this as a shift in the isothermal equation of state to include a constant offset:

$$p = \rho c_s^2 + p_0, \quad (31)$$

which does not change the solution of the isothermal, cylindrical Lane-Emden equation, as the hydrostatic equilibrium depends only on the gradient of the pressure. The scaling of the profile does not change and thus the maximum line-mass remains the same.

This effect can also be seen in the radial density profile in Figure 9. Here we show the measured density averaged over all slices along the filament as the solid red line. Additionally, we overplot the different expected density profiles, once with a turbulent pressure contribution as given in Equation 27 shown as the dotted line and once without an additional pressure as given by the dashed line. For both cases we use the central density to normalise the scale height. One can see that the measured profile follows the

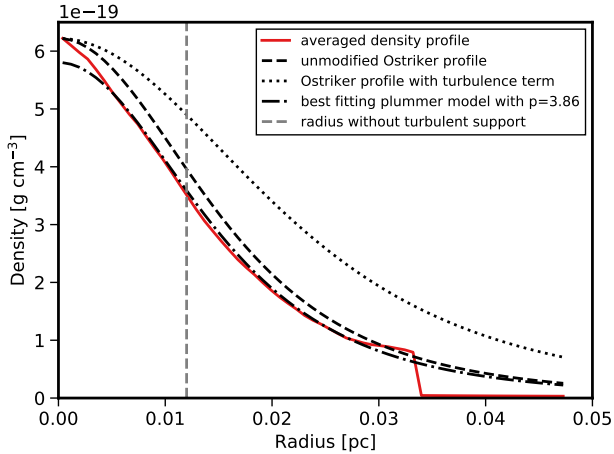


Figure 9. The measured density profile constructed from averaged radial bins of our fiducial filament at 0.5 Myrs, the timestep when the radius reaches its maximum extent. The black dashed line shows the measured density of the filament gas while the dashed and dotted gray lines show the corresponding density profiles using the same central density as the measured profile. The dashed line is given by the unchanged Ostriker scaling and the dotted line is given by including an additional pressure contribution. The dashed-dotted gray line shows the best fitting plummer model with an exponent of -3.86. We also show the radial extent we would expect without any turbulent pressure contribution as given by the dashed black line (see also Figure 6).

unmodified density almost perfectly albeit there is a slight offset due to what seems to be a small over-density in the centre of the filament skewing the resulting profile. In order to check if the accretion changes the slope of the profile, we also fit a plummer profile to the measured density which is free to vary in the central density, in the scale height and in power. The best fitting model is given by the dashed-dotted line and shows an exponent of 3.86 which is very close to the analytic value of 4. Thus, the profile is softened barely by the accretion process. As the boundary pressure of the filament is larger, it extends further into the surrounding medium. This is demonstrated by the vertical dashed black line which shows the extent of the filament we would expect lacking any internal turbulent pressure. Note, that turbulence thus can influence the absolute value of the scale height by setting the central density via the radial extent, but it does not change the general scaling of the profile and therefore is not added as isotropic pressure contribution to the sound speed.

5 THEORETICAL IMPLICATIONS FOR CORE FORMATION

In all our simulations independent of the inflow Mach number, the radial velocity dispersion at the filament boundary amounts to about 0.85 times the total equilibrium velocity dispersion of the non self-gravitational case for which a functional form can be found in the appendix. Thus, we can calculate the theoretical radius and central density of the filament at every line-mass and therefore we can make

predictions on the fragmentation length and time-scales of cores forming in an accreting filament using the gravitational fragmentation model. This model was successfully applied to explain several observed core distances (Jackson et al. 2010; Miettinen 2012; Busquet et al. 2013; Beuther et al. 2015; Contreras et al. 2016; Heigl et al. 2016; Kainulainen et al. 2016) however it is not able to explain all observations (André et al. 2010; Kainulainen et al. 2013; Takahashi et al. 2013; Lu et al. 2014; Wang et al. 2014; Henshaw et al. 2016; Teixeira et al. 2016; Kainulainen et al. 2017; Lu et al. 2018; Palau et al. 2018; Williams et al. 2018; Zhou et al. 2019). It predicts that small density perturbations in the linear regime along the filament axis of the form:

$$\rho(r, x, t) = \rho_0(r) (1 + \epsilon \exp(ikx - i\omega t)) \quad (32)$$

will grow for values of k where the dispersion relation $\omega^2(k)$ is negative. Here ρ_0 is the unperturbed initial density, $k = 2\pi/\lambda$ is the wave vector with λ being the perturbation length, x is the filament axis, $\omega = 1/\tau$ is the growth rate with τ being the growth timescale, t the time variable and ϵ the perturbation strength. The fastest growing, or dominant, fragmentation length scale λ_{dom} as well as the growth timescale of the dominant mode τ_{dom} depend on the current line-mass as well as the current central density of the filament and are given by the pre-calculated (Nagasawa 1987) and interpolated values in Fischera & Martin (2012), shown by their table E.1. We use these values to determine the length scale of the fastest growing mode at every line-mass for the same mass accretion rate but for different inflow Mach numbers as shown in Figure 10. As one can see, the dominant fragmentation length changes over the evolution of the line-mass. At the boundary values it vanishes to zero and it has a maximum at about $f_{\text{cyl}} = 0.4$. The figure is self-similar for different mass accretion rates, with a lower rate leading to a larger dominant fragmentation length. For a constant accretion rate, the fragmentation length does not vary much for different inflow Mach numbers. Only for large and for very low inflow Mach numbers, the fragmentation length is slightly larger. As the dominant fragmentation length is constantly changes as f_{cyl} grows, it is hard to make predictions of what will be the final distance between forming cores. But the curves have a maximum which allows us to make a prediction about the minimum number of cores that will form. For instance, a filament with an inflow Mach number of 4.0 and a length of 0.2 pc will form at least one core. As soon as the first core forms, the further evolution of the filament is also influenced by the gravitational attraction of the core. This makes the formation of additional cores even more unpredictable.

We can get some further constraints from calculating the core growth time. As the filament grows in mass, we assume that cores are seeded at each line-mass on the temporary dominant wavelength with a perturbation strength of 0.09 given by the standard deviation of observed line-masses in the study by Roy et al. (2015). In order for cores to be observed at a certain distance, the cores have to grow faster than the filament itself lest their local line-mass enhancement is overtaken by the overall line-mass growth of the filament. The limit of this growth is the critical line-mass where the cores locally collapse radially and which value they have to reach before the overall filament in order to be observable as cores. Therefore, we compare the timescale of the overall filament to reach the critical line-mass via accre-

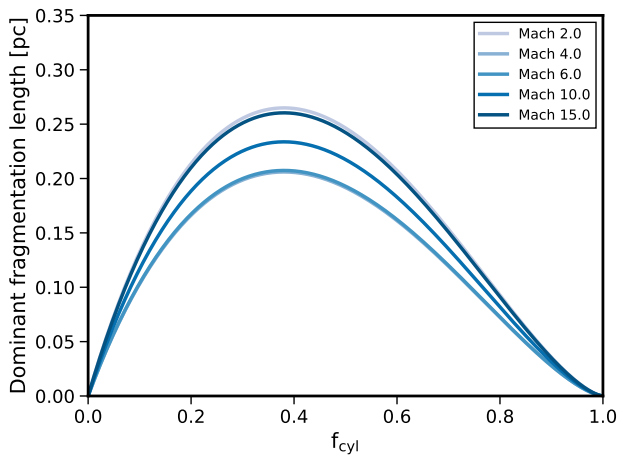


Figure 10. The dominant fragmentation length as a function of the line-mass for the same mass accretion rate of $16.8 M_{\odot} \text{ pc}^{-1} \text{ Myr}^{-1}$ but for different inflow Mach numbers.

tion to the timescale the cores would need to reach this value if they would continue growing on the dominant timescale. This means we solve the equation of the growth of the line-mass for the time t where the line-mass enhancement reaches a value of one:

$$f_{\text{cyl}}^{\text{max}}(t) = f_{\text{cyl}}^0 (1 + \epsilon \exp(t/\tau_{\text{dom}})) = 1.0, \quad (33)$$

where f_{cyl}^0 is the unperturbed line-mass at the beginning of the growth of the respective fastest growing mode. One also has to assume a perturbation strength ϵ which we set to 0.09 as mentioned above. Note, that the dominant timescale grows to longer values as the filament evolves as it is only dominant for the initial line-mass where the cores start growing. Therefore, our calculation represents the most optimistic case and the time to reach the critical line-mass is only a lower boundary.

The result of this calculation is shown in Figure 11. The filament is accreting mass at a constant rate, thus the time for to reach the maximum line-mass is decreasing linearly as shown by the black dotted line. As one can see, the growth timescale of a core is larger than the filament collapse time for the majority of its evolution. The dominant growth timescale is shorter for large central densities as is the case at very low and high values of f_{cyl} where the filament is centrally concentrated. The upper value of f_{cyl} where the growth time curves intersect the collapse timescale of the filament is approximately where we also typically observe core formation in our simulations. For lower values of f_{cyl} we never see any core formation occurring. We do see local overdensities on very small length scales similar to random noise but no real core forms. As the dominant length scale changes over time, any pre-existing overdensity is washed out. This changes for high line-masses as here the cores form local overdensities which large gravitational attraction suppresses the further change of the dominant mode. The timescale to reach the critical line-mass is very small and the collapse of the core is irreversible.

However, filaments of seed line-masses of values lower than 0.5 theoretically could never reach the critical line-mass

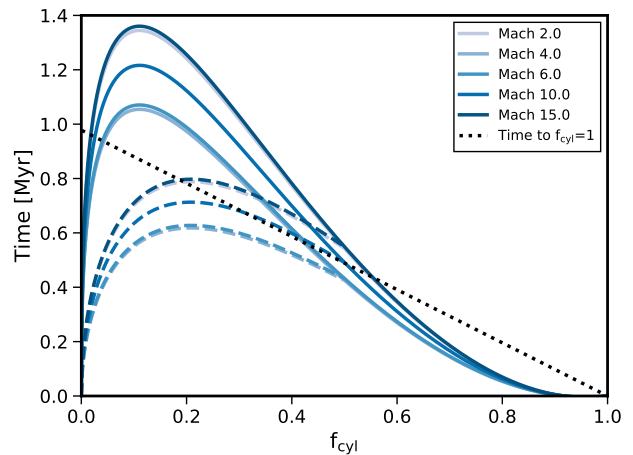


Figure 11. The dominant fragmentation time compared to the collapse time of a filament as a function of the line-mass. The dashed line shows the remaining time to reach a value of $f_{\text{cyl}} = 1.0$ compared to the time it takes a growing core to reach the same value at each line-mass. Only at values of $f_{\text{cyl}} \approx 0.7$ and above, cores have time to form before the filament collapses.

in the linear regime as the linear model allows at most an increase of the local line-mass of a factor of two. There are non-linear effects where it could accrete mass from all over the filament (Heigl et al. 2016) but here we assume it continues to grow in the linear regime and the additional mass is provided by the filament accretion. Nevertheless, we also show the timescales to reach the theoretical maximum local line-mass given by the dashed lines. Note, that if we calculate the timescale the overall filament needs to reach the same value from the same initial line-mass, it is always faster than the cores themselves.

As in the case of the fragmentation length, the growth timescale is self-similar. A larger mass accretion rate only shortens the growth time as well as the time for the filament to reach the maximum line-mass in the same manner. Note, that this relation therefore also holds true for an increasing inflow velocity due to a growing line-mass. This implies that if cores are observed in an accreting filament, it is more likely to have a line-mass closer to the maximum line-mass. From the results of Heigl et al. (2018b) which show that cores forming in high line-mass filaments lead to a reduced filament radius at the position of the core, we also expect the cores to have a thinner morphology than the filament itself.

6 DISCUSSION AND CONCLUSIONS

This work presents a numerical study on accretion driven turbulence in filaments. Together with the results of paper I, we have shown that, depending on inflow velocity, accretion flows with realistic inflow velocities and observed mass accretion rates can drive turbulent motions ranging from subsonic to supersonic velocities. The major difference to the former study without gravity is a limited filament radius and an associated decaying velocity dispersion. Moreover, accretion driven turbulence leads to a radial profile of the velocity dis-

persion which is anti-correlated to the density profile, thus resulting in a constant turbulent pressure throughout the filament and therefore to a lack of turbulent pressure support. However, our model relies on several assumptions.

First of all, our simulations lack magnetic fields which could suppress turbulent motions. Although magnetic fields are thought of channelling accretion flows along striations, density enhancements perpendicular to the filament (Goldsmith et al. 2008; Palmeirim et al. 2013; Cox et al. 2016), they have been shown to stabilise filament against fragmentation depending on the field configuration (Stodólkiewicz 1963; Nagasawa 1987; Gehman et al. 1996b; Fiege & Pudritz 2000b). They can act as an additional pressure support and also suppress motions perpendicular to the field lines. The effects of magnetic fields therefore will be explored in a future paper.

Furthermore, while we do include an initial density perturbation in order to break the symmetry, our accretion flow is very smooth. It could be that accretion is better treated by the infall of clumpy material or even with initial turbulent velocity distributions as in Clarke et al. (2017). Filaments do not form in isolation and driven turbulent box simulations show filaments forming as transient entities (Federrath 2016). To that end, large scale simulations with realistic inflows in an molecular cloud environment are needed which are out of the scope of this work.

Observations of the massive filament DR21 show an increasing velocity dispersion toward the central axis of the filament (Schneider et al. 2010). Our models shows a decreasing velocity dispersion towards the centre of the filament. However, one has to take projection effects into account. While mock observations of our models do not show an obvious increase, we also do not see any systematic drop of velocity dispersion towards the centre of the filament either. However, it could be that the potential of a comparison is limited as DR21 is supercritical and probably in a state of radial collapse.

Nevertheless, all our simulations show the lack of turbulent pressure support against radial collapse independent of inflow Mach number. This constitutes an interesting case where turbulence does not act as an additional pressure. We can summarise our findings as the following:

- A smooth radial accretion onto filaments drives turbulent motions which are radially dominated and decay over time.
- The turbulent pressure has a radial profile which is anti-correlated to the density as the low density outer layers are easier to stir.
- This leads to a constant turbulent pressure component which does not add radial stability as the stability relies on pressure gradients.
- We predict that cores usually form for higher line-mass in accreting filaments ($f_{\text{cyl}} \geq 0.5$) as only then their growth is fast enough to outpace the collapse of the entire filament.

ACKNOWLEDGEMENTS

We thank Alvaro Hacar and the whole CAST group for helpful comments and discussions. Furthermore, we thank the referee for improving the quality of the paper. AB, MG and SH have been supported by the priority programme 1573

”Physics of the Interstellar Medium” of the German Science Foundation and the Cluster of Excellence ”Origin and Structure of the Universe”. The simulations were run using resources of the Leibniz Rechenzentrum (LRZ, Munich; linux cluster CoolMUC2).

REFERENCES

- André P., et al., 2010, *A&A*, **518**, L102
- André P., Di Francesco J., Ward-Thompson D., Inutsuka S.-I., Pudritz R. E., Pineda J. E., 2014, *Protostars and Planets VI*, pp 27–51
- Arzoumanian D., et al., 2011, *A&A*, **529**, L6
- Arzoumanian D., André P., Peretto N., Könyves V., 2013, *A&A*, **553**, A119
- Beuther H., Ragan S. E., Johnston K., Henning T., Hacar A., Kainulainen J. T., 2015, *Astronomy and Astrophysics*, **584**, A67
- Busquet G., et al., 2013, *ApJ*, **764**, L26
- Clarke S. D., Whitworth A. P., Duarte-Cabral A., Hubber D. A., 2017, *MNRAS*, **468**, 2489
- Clarke S. D., Whitworth A. P., Spowage R. L., Duarte-Cabral A., Suri S. T., Jaffa S. E., Walch S., Clark P. C., 2018, *MNRAS*, **479**, 1722
- Contreras Y., Garay G., Rathborne J. M., Sanhueza P., 2016, *Monthly Notices of the Royal Astronomical Society*, **456**, 2041
- Cox N. L. J., et al., 2016, *A&A*, **590**, A110
- Elmegreen B. G., Burkert A., 2010, *ApJ*, **712**, 294
- Fatuzzo M., Adams F. C., 1993, *ApJ*, **412**, 146
- Federrath C., 2016, *MNRAS*, **457**, 375
- Fiege J. D., Pudritz R. E., 2000a, *MNRAS*, **311**, 85
- Fiege J. D., Pudritz R. E., 2000b, *MNRAS*, **311**, 105
- Fischera J., Martin P. G., 2012, *A&A*, **542**, A77
- Gehman C. S., Adams F. C., Fatuzzo M., Watkins R., 1996a, *ApJ*, **457**, 718
- Gehman C. S., Adams F. C., Watkins R., 1996b, *ApJ*, **472**, 673
- Goldsmith P. F., Heyer M., Narayanan G., Snell R., Li D., Brunt C., 2008, *ApJ*, **680**, 428
- Hacar A., Tafalla M., 2011, *A&A*, **533**, A34
- Hacar A., Tafalla M., Kauffmann J., Kovács A., 2013, *A&A*, **554**, A55
- Hacar A., Kainulainen J., Tafalla M., Beuther H., Alves J., 2016a, *A&A*, **587**, A97
- Hacar A., Alves J., Burkert A., Goldsmith P., 2016b, *A&A*, **591**, A104
- Hacar A., Tafalla M., Forbrich J., Alves J., Meingast S., Grosschedl J., Teixeira P. S., 2018, *A&A*, **610**, A77
- Heigl S., Burkert A., Hacar A., 2016, *MNRAS*, **463**, 4301
- Heigl S., Burkert A., Gritschneider M., 2018a, *MNRAS*, **474**, 4881
- Heigl S., Gritschneider M., Burkert A., 2018b, *MNRAS*, **481**, L1
- Heitsch F., 2013, *ApJ*, **769**, 115
- Heitsch F., Ballesteros-Paredes J., Hartmann L., 2009, *ApJ*, **704**, 1735
- Henshaw J. D., et al., 2016, *MNRAS*, **463**, 146
- Hubber D. A., Rosotti G. P., Booth R. A., 2018, *MNRAS*, **473**, 1603
- Jackson J. M., Finn S. C., Chambers E. T., Rathborne J. M., Simon R., 2010, *ApJ*, **719**, L185
- Kainulainen J., Ragan S. E., Henning T., Stutz A., 2013, *Astronomy and Astrophysics*, **557**, A120
- Kainulainen J., Hacar A., Alves J., Beuther H., Bouy H., Tafalla M., 2016, *A&A*, **586**, A27
- Kainulainen J., Stutz A. M., Stanke T., Abreu-Vicente J., Beuther H., Henning T., Johnston K. G., Megeath S. T., 2017, *A&A*, **600**, A141

Kirk H., Myers P. C., Bourke T. L., Gutermuth R. A., Hedden A., Wilson G. W., 2013, *ApJ*, **766**, 115

Klessen R. S., Hennebelle P., 2010, *A&A*, **520**, A17

Kolmogorov A., 1941, *Akademiia Nauk SSSR Doklady*, **30**, 301

Kritsuk A. G., Lee C. T., Norman M. L., 2013, *MNRAS*, **436**, 3247

Larson R. B., 1981, *MNRAS*, **194**, 809

Lizano S., Shu F. H., 1989, *ApJ*, **342**, 834

Lu X., Zhang Q., Liu H. B., Wang J., Gu Q., 2014, *ApJ*, **790**, 84

Lu X., et al., 2018, *The Astrophysical Journal*, **855**, 9

Mac Low M.-M., 1999, *ApJ*, **524**, 169

Mac Low M.-M., Klessen R. S., 2004, *Reviews of Modern Physics*, **76**, 125

Mac Low M.-M., Klessen R. S., Burkert A., Smith M. D., 1998, *Physical Review Letters*, **80**, 2754

Maloney P., 1988, *ApJ*, **334**, 761

McKee C. F., Zweibel E. G., 1995, *ApJ*, **440**, 686

McLaughlin D. E., Pudritz R. E., 1997, *ApJ*, **476**, 750

Miettinen O., 2012, *Astronomy and Astrophysics*, **540**, A104

Moeckel N., Burkert A., 2015, *ApJ*, **807**, 67

Nagasawa M., 1987, *Progress of Theoretical Physics*, **77**, 635

Ostriker J., 1964, *ApJ*, **140**, 1056

Padoan P., Nordlund Å., 1999, *ApJ*, **526**, 279

Padoan P., Pan L., Haugbølle T., Nordlund Å., 2016, *ApJ*, **822**, 11

Palau A., et al., 2018, *The Astrophysical Journal*, **855**, 24

Palmeirim P., et al., 2013, *A&A*, **550**, A38

Roy A., et al., 2015, *A&A*, **584**, A111

Schneider N., Csengeri T., Bontemps S., Motte F., Simon R., Hennebelle P., Federrath C., Klessen R., 2010, *A&A*, **520**, A49

Smith R. J., Glover S. C. O., Klessen R. S., 2014, *MNRAS*, **445**, 2900

Smith R. J., Glover S. C. O., Klessen R. S., Fuller G. A., 2016, *MNRAS*, **455**, 3640

Stodólkiewicz J. S., 1963, *Acta Astron.*, **13**, 30

Stone J. M., Ostriker E. C., Gammie C. F., 1998, *ApJ*, **508**, L99

Tafalla M., Hacar A., 2015, *A&A*, **574**, A104

Takahashi S., Ho P. T. P., Teixeira P. S., Zapata L. A., Su Y.-N., 2013, *ApJ*, **763**, 57

Teixeira P. S., Takahashi S., Zapata L. A., Ho P. T. P., 2016, *Astronomy and Astrophysics*, **587**, A47

Teyssier R., 2002, *A&A*, **385**, 337

Toro E., Spruce M., Speares W., 1994, *Shock Waves*, **4**, 25

Truelove J. K., Klein R. I., McKee C. F., Holliman II J. H., Howell L. H., Greenough J. A., 1997, *ApJ*, **489**, L179

Wang K., et al., 2014, *Monthly Notices of the Royal Astronomical Society*, **439**, 3275

Williams G. M., Peretto N., Avison A., Duarte-Cabral A., Fuller G. A., 2018, *Astronomy and Astrophysics*, **613**, A11

Zamora-Avilés M., Ballesteros-Paredes J., Hartmann L. W., 2017, *MNRAS*, **472**, 647

Zhou C., Zhu M., Yuan J., Wu Y., Yuan L., Moore T. J. T., Eden D. J., 2019, *Monthly Notices of the Royal Astronomical Society*, **485**, 3334

van Leer B., 1977, *Journal of Computational Physics*, **23**, 276

van Leer B., 1979, *Journal of Computational Physics*, **32**, 101

APPENDIX A: NON SELF-GRAVITATIONAL RADIUS EVOLUTION REVISITED

While we found a linear relation between the inflow velocity and the equilibrium velocity dispersion in paper I, we could not find a reasonable explanation for the offset of the linear fit. As we have refined our measurement techniques and up-

dated our model, we want to discuss the implications of this study on our previous work.

A1 Radial evolution without self-gravity

As the density inside the filament is constant in the non self-gravitational case, we formerly modeled the radius by the mass accretion rate (Equation 12) assuming that the mean density inside the filament is given by the exterior density times the square of the Mach number in an isothermal shock:

$$\langle \rho \rangle_{\text{fil}} = \rho_{\text{ext}} \mathcal{M}_a^2. \quad (\text{A1})$$

The mass accretion rate together with the total mass of the filament

$$M = \pi R^2 L \langle \rho \rangle_{\text{fil}} = \pi R^2 L \rho_{\text{ext}} \mathcal{M}_a^2 = \pi R L \rho_0 R_0 \mathcal{M}_a^2, \quad (\text{A2})$$

then leads to a radius evolution given by

$$R(t) = \frac{2c_s^2 t}{v_a}. \quad (\text{A3})$$

While we found a good agreement, this does not take into account the effect of turbulence on the radius. A better model is to consider the pressure equilibrium at the filament boundary, analogous to Equation 15, supported internally by the turbulent pressure $\langle \rho \rangle_{\text{fil}} \sigma^2$ and by the ram pressure $\rho_{\text{ext}} v_a^2$ on the outside:

$$\langle \rho \rangle_{\text{fil}} (c_s^2 + \sigma^2) = \rho_{\text{ext}} (c_s^2 + v_a^2). \quad (\text{A4})$$

This gives the internal mean density

$$\langle \rho \rangle_{\text{fil}} = \rho_{\text{ext}} \frac{(1 + \mathcal{M}_a^2)}{(1 + \mathcal{M}_t^2)} \quad (\text{A5})$$

which leads to the radius evolution of

$$R(t) = 2v_a t \frac{(1 + \mathcal{M}_t^2)}{(1 + \mathcal{M}_a^2)}. \quad (\text{A6})$$

As we have shown in Figure 4 the turbulence inside the filament is not isotropic. Thus, it is not necessarily the total velocity dispersion which supports the internal pressure. Furthermore, it is important to note that the hydrostatic equilibrium is given by the turbulent pressure at the boundary. As the non self-gravitating velocity dispersion has a similar radial profile as shown for the self-gravitating case in Figure 5, we would need to use the boundary velocity dispersion value in Equation A6. However, for the non self-gravitational case, the boundary velocity dispersion is very similar to the velocity dispersion calculated from the total filament as it does not have a density profile. Therefore, we do not see an anti-correlation between density and velocity dispersion and the latter is then dominated by the largest value which is at the boundary. We plot the radial evolution as solid red line in Figure A1 together with the expected evolution including no turbulent support as dashed, only radial support as dashed-dotted and total turbulence support as dotted black line. Compared to paper I, we improved our measurement method of the radius by not using the largest density jump but by using the same methodology as we do for the velocity dispersion which distinguishes filament material from the

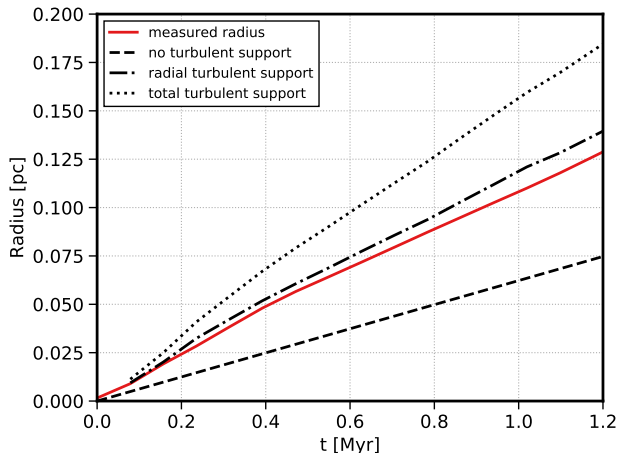


Figure A1. Radial evolution of a filament with a Mach 6 inflow without gravity. The solid black line is the measured radius at each time step. The theoretical predictions are given by Equation A6 with the full, radial and no turbulent support is given by the dotted, dashed-dotted and dashed line respectively.

surrounding by using the drop in radial velocity. We found that the density inside the filament can vary substantially and the largest density jump does underestimate the filament radius. Moreover, sometimes the filament can be deformed, having a more elliptical formed cross-section. We reduce the impact of this effect by using the mean radius of two perpendicular cuts through the center of the filament. The expected evolution follows from Equation A6 together with the measured velocity dispersion at every time-step. Note that the no turbulent support case is indistinguishable from the isothermal shock radial evolution of Equation A3 for large inflow Mach numbers.

As one can see, the radius is best fitted by a support of the radial component of the velocity dispersion. This shows that only radial motions of the filament are important in setting the boundary pressure against the radial inflow.

A2 Equilibrium velocity dispersion

We now want to use the information about the non self-gravitational radius evolution to explain the linear relationship we found in paper I between the inflow velocity and the created turbulence. We measure the equilibrium value which we plot as red data points in Figure A2. The left panel shows the direct relationship between the inflow velocity and the generated turbulence. On the right hand side we plot the same values but squared in order to compare the inflow energy to the turbulent energy. Additionally, we show the values of the radial turbulence as blue squares. The error bars indicate that not all simulations give the same equilibrium number but different seeds in the random density distribution result in slightly different equilibrium values with a spread of about 10%. However, this error does not enter our fit to the datapoints. In gray, we also plot the data values of paper I which were calculated using the density weighted standard deviation. One can see that for low values the differences are not huge but they become increas-

ingly larger for higher inflow Mach numbers, as discussed at the beginning of section 4. Compared to paper I, we also extend the range of inflow velocities to Mach 15 which is already much greater than the expected values but serves as a good upper limit.

The reason why in general there is an equilibrium level in the velocity dispersion in the non-gravitational case is due to Equation 25. If the radius is growing linearly with time as shown in Equation A6 and if the equilibrium has been established, the dissipation rate is constant in time (Equation 20):

$$\dot{E}_d \approx \frac{1}{2} \frac{M(t)\sigma^3}{L_d(t)} = \frac{1}{2} \frac{\dot{M}t\sigma^3 (1 + \mathcal{M}_a^2)}{4v_{at} (1 + \mathcal{M}_t^2)} = \frac{\dot{M}\sigma^3 (1 + \mathcal{M}_a^2)}{8v_a (1 + \mathcal{M}_t^2)}. \quad (\text{A7})$$

If the velocity dispersion is greater than the equilibrium value, the excess is dissipated away, if it is lower, less energy is dissipated. Thus it will settle at a value where the dissipation is constant.

In order to compare to theoretical models we first discuss the prediction by Heitsch (2013). It assumes that one can express the dissipation rate as a constant fraction of the constant energy inflow (Equation 22):

$$\epsilon = \left| \frac{\dot{E}_d}{\dot{E}_a} \right|. \quad (\text{A8})$$

Note that ϵ can only be constant in time for a constant mass accretion rate if the dissipation rate is constant in time. For a non-linear radial evolution this is not the case. Furthermore, the model assumes that ϵ is independent of the inflow velocity which is not necessarily true as the fraction of accreted energy converted to turbulent motions can change with the inflow velocity. Nevertheless, in the non-gravitational case Equation 23 transforms to

$$\frac{\mathcal{M}_t^3}{(1 + \mathcal{M}_t^2)} = \frac{4\epsilon\mathcal{M}_a^3}{(1 + \mathcal{M}_a^2)}. \quad (\text{A9})$$

As turbulence is generated in oblique shocks on the surface of the filament, we need supersonic inflow motions. Below an inflow velocity of Mach 1.0 we do not generate turbulent motions or even form a pressure bound filament. Therefore, we shift the zero point of Equation A9 to an inflow velocity of Mach 1.0 by effectively applying the transformation $\mathcal{M}'_a = \mathcal{M}_a - 1$. Note that this transformation only affects the energy accretion term and not to the evolution of the radius. Thus, the equation is now:

$$\frac{\mathcal{M}_t^3}{(1 + \mathcal{M}_t^2)} = \frac{4\epsilon\mathcal{M}_a'^2\mathcal{M}_a}{(1 + \mathcal{M}_a'^2)}. \quad (\text{A10})$$

A realistic estimate of ϵ is expected to lie between 5% and 10% (Klessen & Hennebelle 2010) which we plot as the dashed-dotted light blue and red lines respectively. As one can see the curves do not fit the measured points and fit even worse if we do not apply the transformation. The shape of the curve cannot be matched to the data points even if we fit different values of ϵ . This leaves us with the conclusion that ϵ is only a constant in time for a certain inflow velocity but varies with the inflow velocity.

As we clearly cannot apply the model by Heitsch (2013),

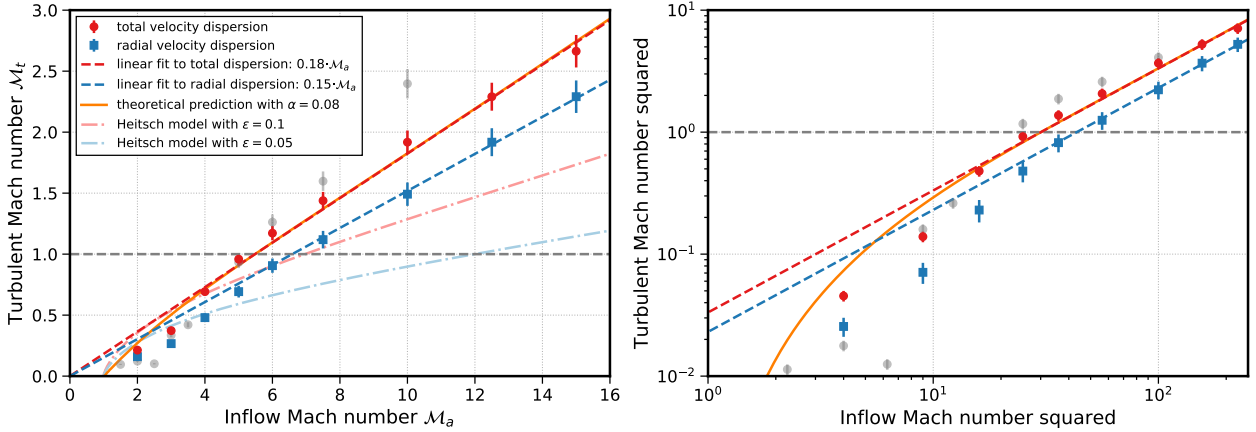


Figure A2. Equilibrium values of accretion driven turbulence in dependence of the inflow Mach number. Both plots show the same data points. On the left hand side we directly plot the values which we calculate from the kinetic energy. The gray data points are the values of the density weighted standard deviation we used in paper I. On the right hand side we show the same data points with squared values in log-log scale.

we try to fit Equation 25 directly. If we insert the evolution of the non self-gravitational radius, it transforms to

$$\mathcal{M}_t^2 = \alpha \mathcal{M}_a^2 - \frac{\mathcal{M}_t^3 (1 + \mathcal{M}_a^2)}{4\mathcal{M}_a (1 + \mathcal{M}_t^2)}. \quad (\text{A11})$$

We fit this relation in Figure A2 as solid, orange line and get the best fitting value of $\alpha = 0.085$. As one can see it follows the data points well and has the same scaling for large \mathcal{M}_a . Only for low inflow Mach numbers there is some discrepancy where the data points lie not exactly on the relation. Therefore, our model seems to reasonably explain the connection of accretion driven turbulence an inflow Mach number.

Nevertheless, our simulations show that most of the inflow energy is lost. In the accretion process only 8.5% of the energy is kept in the shock phase and if we convert the linear fit to the total velocity dispersion to an energy relation, it indicates that from this value only only about $0.18^2 = 3.2\%$ of the energy is retained in turbulent motions at equilibrium for large inflow Mach numbers. The energy difference between these two values is lost in the continuous dissipation inside the filament.

This paper has been typeset from a $\text{\TeX}/\text{\LaTeX}$ file prepared by the author.